Filamentation of femtosecond radiation from a Cr : forsterite laser in air

M.B. Agranat, V.P. Kandidov, P.S. Komarov, A.V. Ovchinnikov, V.Yu. Fedorov

Abstract. **The filamentation of radiation from a 1.24-μm femtosecond Cr : forsterite laser in air is studied experimentally and theoretically. The decrease in the laser beam diameter during filamentation was observed. The parameters of filaments produced by radiation from a Cr : forsterite and a Ti : sapphire lasers are compared. It is shown that a filament produced by radiation from the Cr : forsterite laser appears at a larger distance and contains more energy than a filament produced by radiation from the Ti : sapphire laser with the same initial parameters of pulses.**

Keywords: Cr : forsterite, femtosecond pulses, filamentation.

1. Introduction

The filamentation of high-power femtosecond laser radiation in transparent media is of great interest both for fundamental studies and practical applications. The spatiotemporal localisation of light energy in an extended filament is accompanied by the formation of a laser plasma, generation of a supercontinuum, and amplification of the nonlinear-optical interaction of radiation with a medium. The unique properties of filamentation extend qualitatively the field of applications of laser methods in scientific studies and open up new possibilities for femtosecond laser technologies in atmospheric optics, microoptics, and other fields [1 – 5]. A femtosecond lidar, in which a broadband source of directed radiation is the supercontinuum of filaments, combines the advantages of time-resolved probing and differential absorption spectroscopy. Fluorescence spectroscopy based on multiphoton excitation by the intense field of filaments is used for remote probing of pollutants in the atmosphere [6, 7], while emission spectroscopy involving the generation of a filament plasma on a target surface is applied for determining the elemental composition of remote objects [8, 9]. A filament plasma channel can be used for the remote control of a high-voltage discharge, in particular, to provide the sink of atmospheric electricity [10, 11]. The photoinduced micro-modification of a dielectric medium by a filament is a new method for recording waveguides, couplers, diffraction gratings, and other elements of microoptics in optical materials [12]. The application of filamentation in concrete laser technology imposes certain requirements on filament parameters and, hence, on femtosecond laser radiation. Thus, at present the influence of the initial phase modulation and radiation focusing of the supercontinuum generation efficiency [13], the formation of plasma channels [14], and the position of filaments [15] during the propagation of laser pulses along extended atmospheric paths is being actively investigated.

The filamentation phenomenon is studied experimentally and theoretically mainly at the wavelength 800 nm of most popular femtosecond lasers with a Ti : sapphire crystal output amplifier [2 – 4]. In experiments on the filamentation of visible and UV radiation in air, the second harmonic of a neodymium laser, the seconds and third harmonics of a Ti : sapphire laser, and radiation from excimer lasers are used. The extended filamentation of 40-GW [16] and 32-TW [17] subpicosecond pulsed radiation from neodymium glass lasers in air was observed. The third harmonic generation in air was observed upon filamentation of radiation at 1.54 μm obtained due to parametric conversion of radiation from a Ti : sapphire laser [18].

In this paper, we present the results of experimental and theoretical studies of filamentation in air of radiation from a 1.24-μm femtosecond Cr : forsterite laser. The energy density in a filament and its radius are determined. The parameters of filaments produced by radiation from Cr : forsterite and T : sapphire lasers are compared.

2. Experimental

Experiments were performed by using a femtosecond Cr : forsterite laser system developed at the JIHT, RAS [19]. A Z-cavity master oscillator generates 1.24-μm femtosecond pulses with a FWHM of 50 nm. The average output power is 200 mW and the pulse energy achieves 2.3 nJ. Femtosecond laser pulses are amplified by the method of amplification of chirped pulses. The Cr : forsterite laser system uses a stretcher with one diffraction grating which provides the increase in the pulse duration by three order of magnitudes. The stretcher efficiency (the output/input pulse energy ratio) is ∼ 60 %.

As the first amplification stage, a regenerative amplifier (RA) with a ring cavity is used [20]. An advantage of the

M.B. Agranat, P.S. Komarov, A.V. Ovchinnikov Joint Institute for High Temperatures, Russian Academy of Sciences, ul. Izhorskaya 13-2, 125412 Moscow, Russia; e-mail: ovtch2006@rambler.ru;
V.P. Kandidov, V.Yu. Fedorov Department of Physics, M.V. Lomonosov Moscow State University, Vorob'evy gory, 119992 Moscow, Russia; e-mail: kandidov@phys.msu.ru

ring cavity used in the RA compared to popular linear cavities is the absence of optical isolation between the amplifier and master oscillator, which is usually achieved with the help of a Faraday cell. The radiation of the RA with a ring cavity has the double contrast compared to the RA with a linear cavity [21]. The maximum amplification of a pulse in the RA is achieved after $46-48$ transits in the active medium, and then the pulse is coupled out of the resonator with the help of a controllable Pockels cell. The light pulse energy is increased from 1.4 nJ to 400 μJ, corresponding to the gain of 3×10^5. The intensity contrast, determined from the amplitude ratio of the main pulse and prepulses emerging from the RA, is $\sim 10^3$. The efficient amplification of a single pulse in subsequent amplification stages and the higher contrast required for high-power femtosecond laser systems are obtained by using a scheme for contrast improving, which is placed behind the RA and consists of two crossed polarisers and a Pockels cell located between them. This device improves the intensity contrast between the main pulse and prepulses by three orders of magnitude.

The output pulse energy is further increased in three multipass amplifiers pumped by 1.064-μm, 600-mJ, 10-ns pulses from two Q-switched lasers. The amplified pulse energy achieves 115 mJ. The amplified phase-modulated pulse is compressed in a compressor containing two 600-lines mm^{-1} diffraction gratings of size 100×120 mm. In front of the compressor a telescope with the three-fold magnification is mounted, which provides the energy density on diffraction gratings up to 100 mJ cm^{-2}. The compressor efficiency is 77 %. The laser system emits 1.24-μm, 96 ± 10-fs pulses of energy up to 90 mJ at a repetition rate up to 10 Hz. The system can also emit single pulses triggered manually or by the master oscillator.

Figure 1 presents the scheme of the experimental setup for studying the filamentation of laser radiation. To observe filaments at distances accessible under laboratory conditions, telescope (*2*) was mounted behind the laser system, which reduced the laser beam radius from 6 down to 1.4 mm. A measurement stand for recording the energy density distribution in the beam cross section depending on the pulse energy was placed at fixed distances behind the telescope. Because the energy density in a filament exceeds the damage threshold of opaque screens, the filament image was obtained in the cross-sectional plane by using Fresnel reflection from the external surface of flat glass plate (*4*). This allowed the reduction of the energy density below the damage threshold for optical elements of the measurement equipment. The plate thickness was large enough to avoid the incidence of radiation reflected from its second surface on a CCD camera. The image of the plate surface was magnified by microobjective (*5*) (Plan, LOMO, St. Petersburg, Russia). Then, the reflected radiation passed through a set of neutral filters (*6*) and was incident on CCD camera (*7*) (SensiCam SVGA, PCO AG, Kelheim, Germany). External illumination was rejected with an IR filter mounted close to the CCD camera. Calibrated neutral filters placed behind the microobjective were chosen to provide the complete use of the dynamic range of the CCD camera. The single pulse regime was used in experiments, and the energy density distribution in the beam cross section was recorded by measuring also the pulse energy with the help of calibrated germanium photodiode (*3*).
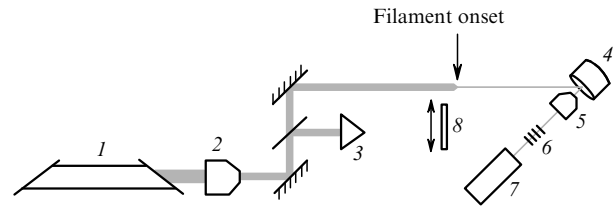

Figure 1. Scheme of the experimental setup: (*1*) laser; (*2*) telescope; (*3*) photodiode (energy meter); (*4*) glass plate; (*5*) microobjective; (*6*) neutral filters; (*7*) CCD camera; (*8*) probe plate.

3. Specific features of the recording of a filament produced by radiation at 1.24 μm

The formation of a filament in air in this case is difficult to observe without the use of a special equipment. Radiation scattered sideways is not observed by the naked eye and its energy is too low to be detected with an IR imager. The electron concentration in the induced plasma is low, and it is difficult to record the plasma recombination emission. The supercontinuum radiation has a small divergence angle, and a distance at which coloured conic emission rings are observed is located far away from the filament formation point. The nonlinear saturation of the IR imager by the intense radiation of the filament and the damage of an opaque screen located in the beam path do not allow one to determine the filament onset position.

To find the filament formation position, we inserted a probe glass plate into the laser beam during the stand adjustment. Filamentation develops in glass at considerably smaller distances than in air, and the divergence angle of conic emission is much larger. The probe plate was inserted into the laser beam directly before the generation of a filament in air, which leads to the formation of a filament in this plate and is accompanied by strongly diverging conic supercontinuum emission, which is distinctly observed by the naked eye. Thus, by moving the glass plate along the laser beam, we can uniquely localise the filament onset position by supercontinuum emission formed directly behind the plate. The accuracy of measuring the distance to the filament onset improves with decreasing the plate thickness. Thus, when a glass plate of thickness 1 mm is used, the systematic error of the lower bound of a distance to the filament formation onset in air is no more than 1 m.

The radiation of Cr : forsterite laser was recorded with a visible CCD camera, in which a signal appears due to multiphoton absorption of IR emission. The CCD camera was calibrated by illuminating it with a broad low-intensity pulsed radiation beam incident directly on the CCD array. Figure 2 presents the dependence of the maximum CCD camera S_{max} over the beam cross section on the pulse energy W. It can be shown that these quantities are related by the expression

$$S_{max} = A W^K, \tag{1}$$

where A is the instrumental function of the measurement path, which depends on the transfer coefficient of optical radiation and spatial and temporal form factors of the laser pulse. Thus, the slope of the dependence $S_{max}(W)$ at the logarithmic scale determines the order K of the multiphoton absorption in the CCD array. The straight line correspond-
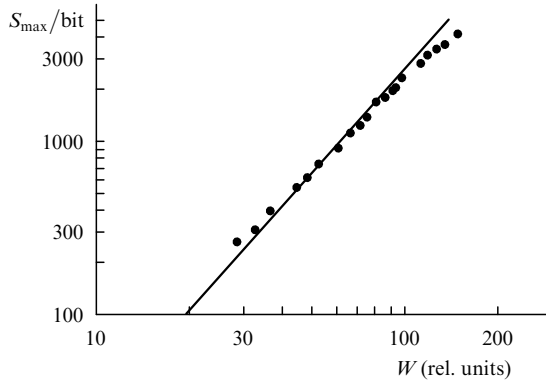
Figure 2. Dependence of the maximum signal S_{max} of the CCD camera on the pulse energy W. The circles are experimental data, the solid straight line in the quadratic approximation.

ing to the function $S_{max} = \text{const} \cdot W^2$ is close to experimental data, which demonstrates the quadratic response of the CCD camera to the 1.24-μm radiation.

The experimental results were processed by using the CCD camera certificate according to which the pixel area Δs on the plate surface is 3.125×3.125 μm^2. The calibration of the CCD camera gave the expression for calculating the peak pulse energy density F_{max} by its energy W and the signal intensity distribution S_{ij} recorded by CCD camera pixels:

$$F_{max} = W\Big[\sum_{i,j} (S_{ij}/S_{max})^{1/K}\Delta s \Big]^{-1}. \qquad (2)$$

The quantitative processing of the images of the energy density distribution in the beam cross section was performed by subtracting from the signal S_{ij} the background noise, which did not exceed 6 bits.

4. Experimental results

The measurement stand was placed in experiments at two fixed states $z = 3.12$ and 5.92 m from the telescope output aperture. For each of the distances, a series of experiments was performed in which the beam image and, hence, the energy density distribution in its cross section were recorded with the CCD camera. The pulse energy was varied from 0.6 to 5.7 mJ, the upper bound being restricted by the radiation resistance of steering mirrors of the experimental setup. Figure 3 presents the typical energy density distributions in the beam cross section for each of these distances. One can see that, as the energy W is increased, the characteristic size of the energy density distribution $F(x, y)$ in the beam cross section decreases. Beginning from some energy, its further increase does not cause the reduction of the transverse size of the image, which demonstrates the formation of a filament.

Note that the initial energy density distribution in the beam cross section is substantially nonunimodal and has a complex structure (Fig. 4). During the filament formation, the self-purification of the beam occurs [22] at which an axially symmetric mode is formed. The images in Fig. 3 obtained at a low pulse energy $W = 1$ mJ exhibit some ellipticity of the energy density distribution. As the pulse energy W is increased, a filament is formed near the recording plane and the distribution $F(x, y)$ becomes axially symmetric. After the formation of a plasma channel, the radiation again becomes nonunimodal. Some photographs, in particular, for $W = 4.34$ mJ at a distance of 3.12 m exhibit the ring-shaped structure of the energy density distribution appearing due to radiation defocusing in the induced laser plasma [23].

The change in the beam radius with increasing pulse energy was determined from the images recorded with the CCD camera. The radius r_{fil} was calculated by using the
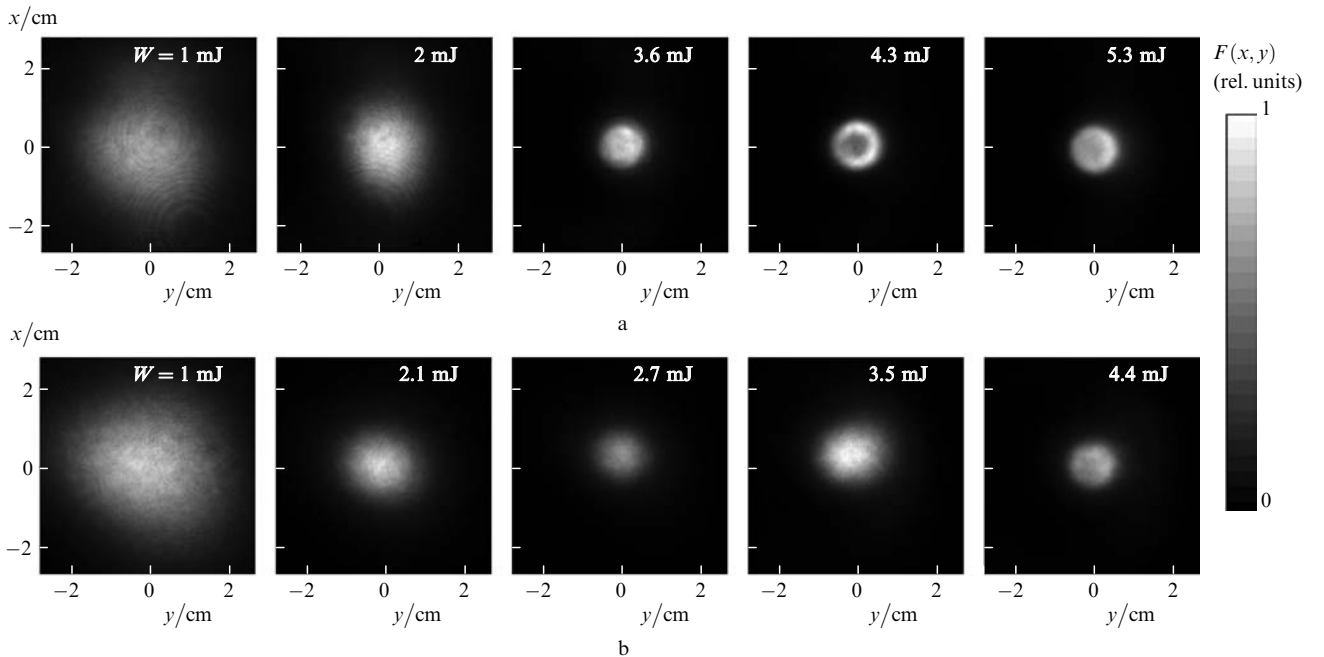

Figure 3. Energy density distributions $F(x, y)$ in the beam cross section recorded with the CCD camera at distances $z = 3.12$ (a) and 5.92 m (b) for different pulse energies W, the pulse duration 96 fs (at the e^{-1} level) and $\lambda = 1.24$ μm. The value of $F(x, y)$ is normalised to the peak value F_{max} for each picture.
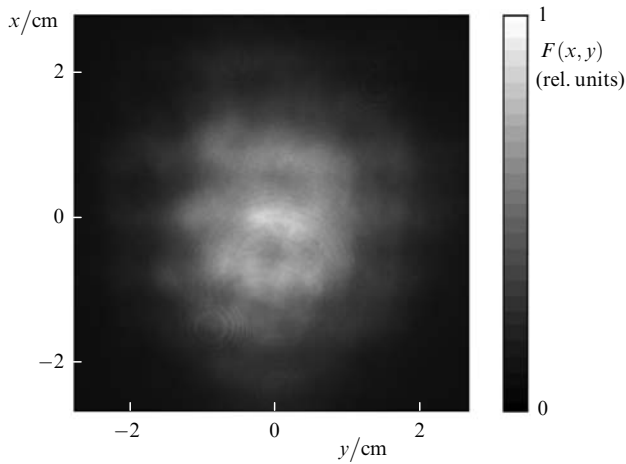
Figure 4. Energy density distribution $F(x, y)$ at the telescope output for the full pulse duration of 96 fs (at the e^{-1} level), $\lambda = 1.24$ μm and the characteristic beam radius of 1.4 mm (at the e^{-1} level). The value of $F(x, y)$ is normalised to the peak value F_{max} at the telescope output.

Gaussian approximation of the energy density distribution in cross sections drawn through the centre of gravity of this distribution. Figure 5 presents the dependences of the beam radius r_{fil} on the energy W for two distances used in experiments. Each experimental point was obtained in one realisation by measuring the pulse energy with photodiode (3). One can see that, as the pulse energy is increased,
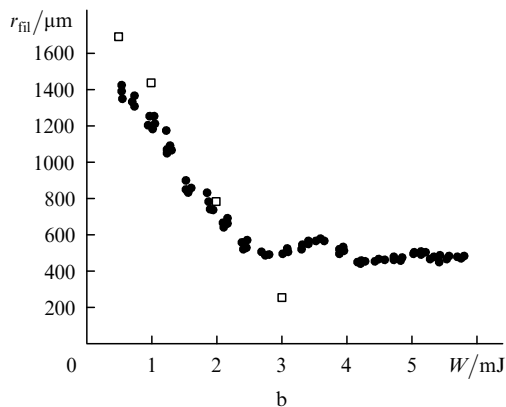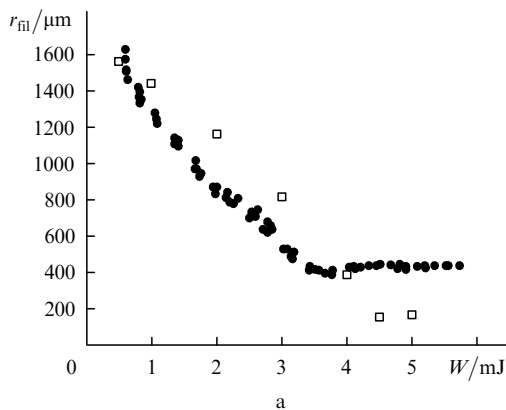
the initially broad beam is compressed and its radius decreases. Beginning from some energy W_{fil}, the radius r_{fil} ceases to decrease, which suggests that a filament is formed in the radiation recording plane. At the distance $z = 3.12$ m, a filament was formed when the pulse energy was $W_{fil} = 3.5$ mJ, and at the distance $z = 5.92$ m, a filament was formed when the pulse energy was 2.5 mJ. The energy density distribution $F(x, y)$ in the filament formation plane has the smallest transverse size (Fig. 3). Then, as the pulse energy was increased, the maxima and minima in the dependence of the filament radius r_{fil} on energy appeared, which corresponds to the refocusing of radiation upon filamentation. Due to pulse defocusing in the induced laser plasma, the radius of the energy density distribution increases. The radiation defocused in the plasma can again contract to the axis, and the transverse size of the energy density distribution will again decrease [23, 24].

Figure 6 presents the dependences of the peak energy density F_{max} in the beam cross section on the pulse energy W for two distances used in experiments. One can see that the peak energy density increases with energy W and this growth stops when some energy density W_{fil} is achieved, which also confirms the formation of a filament. As the pulse energy is further increased, the changing of maxima and minima is observed in the dependence $F_{max}(W)$, which correspond to radiation refocusing in the filament. The number of refocusings observed with increasing pulse energy increased when the measurement stand was located at the greater distance (Fig. 6b). The difference in the dependences

Figure 5. Experimental (●) and calculated numerically (□) dependences of the radius r_{fil} of the energy density distribution in the beam cross section on the pulse energy W for $z = 3.12$ (a) and 5.92 m (b). The radiation parameters are as in Fig. 4.

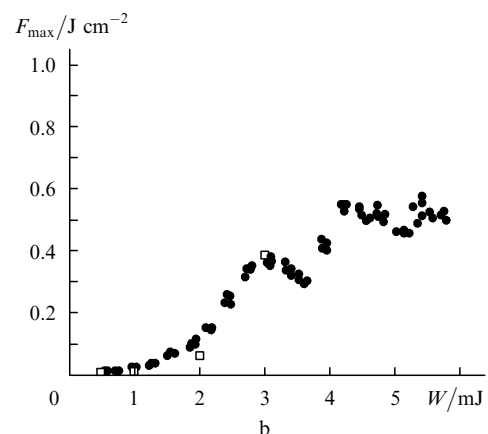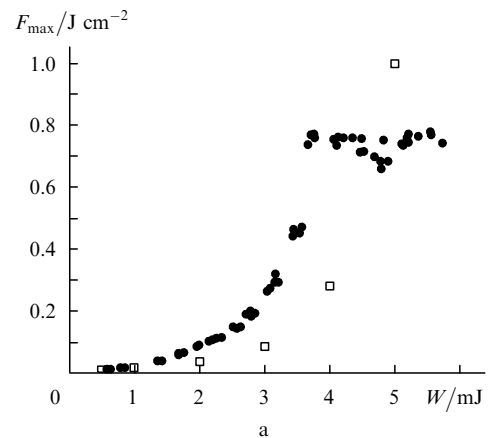**Figure 6.** Experimental (●) and calculated numerically (□) dependences of the energy density F_{max} in the beam on the pulse energy W for $z = 3.12$ (a) and 5.92 m (b). The radiation parameters are as in Fig. 4.

$F_{max}(W)$ for the two distances is explained by the fact that when radiation is detected at a small distance, filamentation only begins, whereas at a large distance the developed filament is recorded.

The energy density in the filament achieves $0.5 - 0.8$ J cm^{-2}. It is important in this case that its relative increase caused by filamentation considerably exceeds the increase in the pulse energy W. Thus, the peak energy density F_{max} increases by 30 times (from 0,025 to 0.74 J cm^{-2}) when the pulse energy is increased by 3.5 times (from 1 to 3.5 mJ). This is explained by the spatial concentration of the pulse energy upon filamentation.

5. Theoretical analysis

The filamentation of high-power femtosecond laser radiation under conditions close to experimental was simulated numerically by using the frequency-dependent model of the nonlinear response of air proposed in [25].

The initial stage of the formation of a filament in femtosecond radiation is caused by the Kerr self-focusing caused by the cubic nonlinearity with the coefficient n_2 depending on the laser radiation wavelength. By now the coefficient n_2 in air for radiation at 1.24 μm is not measured. We determined n_2 (in cm^2 W^{-1}) from the expression [25]

$$n_2(\lambda) = \left(3.00585 + \frac{0.637078}{\lambda^2}\right)10^{-19}, \quad (3)$$

obtained by generalising experimental data, where the wavelength λ is measured in micrometres. According to (3), the cubic nonlinearity coefficient n_2 of air at 0.8 μm is 4×10^{-19} cm^2 W^{-1}, while at 1.24 μm it is somewhat smaller $(3.42 \times 10^{-19}$ cm^2 W$^{-1})$. The critical self-focusing power P_{cr} depends on the wavelength and is described by the expression

$$P_{cr}(\lambda) = 3.77 \frac{\lambda^2}{8\pi n_0 n_2(\lambda)}, \quad (4)$$

where n_0 is the linear refractive index. According to (3) and (4), the critical power for radiation at 0.8 μm is 2.4 GW, whereas at 1.24 μm it is considerably higher, achieving 6.74 GW. The linear refractive index n_0 for radiation at 1.24 μm was determined from the Cauchy formula.

The cubic nonlinearity of air includes the instant contribution of the electronic component and the inertial contribution caused by stimulated scattering by rotational transitions [26]. The contribution of stimulated scattering for femtosecond pulses was calculated by approximating the increment Δn_K of the refractive index caused by cubic nonlinearity by the expression [27, 28]

$$\Delta n_K(x, y, t, z) = \frac{1}{2} n_2 I(x, y, t, z)$$

$$+ \frac{1}{2} n_2 \int_{-\infty}^{t} H(t - t') I(x, y, t', z) dt', \quad (5)$$

where $I(x, y, t, z)$ is the pulse intensity. The expression for the response function $H(t)$ of stimulated Raman scattering has the form [28]

$$H(t) = \theta(t)\Omega^2 \exp\left(-\frac{\Gamma t}{2}\right)\frac{\sin(\Lambda t)}{\Lambda}, \quad (6)$$

where $\theta(t)$ is the Heaviside function; $\Omega = 20.6$ THz and $\Gamma = 26$ THz are the characteristic frequencies for air molecules; and $\Lambda = (\Omega^2 - \Gamma^2/4)^{1/2}$.

The growth of the pulse intensity caused by cubic nonlinearity is stopped by radiation defocusing in the induced laser plasma. The increment of the refractive index caused by the plasma nonlinearity is described by the expression

$$\Delta n_p = -\frac{1}{2n_0}\frac{\omega_p^2}{\omega_0^2}, \quad (7)$$

where $\omega_p^2 = e^2 N_e/(\varepsilon_0 m_e)$ is the square of the plasma frequency; e and m_e are the electron charge and mass, respectively; and ε_0 is the dielectric constant. In (7), the contribution of elastic collisions of electrons with neutral particles is neglected because the collision frequency is considerably lower than the electromagnetic field frequency ω_0. The free electron concentration N_e is determined from the kinetic equation

$$\frac{\partial N_e}{\partial t} = R(I, \lambda)(N_0 - N_e), \quad (8)$$

where $R(I, \lambda)$ is the photoionisation rate depending on the ionisation potential of gas components, the pulse intensity, and laser radiation wavelength; and N_0 is the concentration of neutral air molecules. In air, as a two-component medium, equation (8) is written for nitrogen and oxygen independently. The ionisation rate was calculated by using the Perelomov–Popov–Terent'ev model [29] with the effective charges of nitrogen and oxygen molecular ions determined experimentally [30].

The propagation of high-power femtosecond pulses from a Cr:forsterite laser in air is considered in the approximation of the slowly varying pulse envelope $E(x, y, t, z)$

$$2ik_0\frac{\partial E}{\partial z} = \Delta_\perp E - k_0 k''_\omega \frac{\partial^2 E}{\partial t^2} + \frac{2k_0^2}{n_0}(\Delta n_K + \Delta n_p)E - ik_0\alpha E, \quad (9)$$

where $k_0 = k|_{\omega=\omega_0}$ is the wave number and $k''_\omega = \partial^2 k/\partial\omega^2|_{\omega=\omega_0}$. The first term in the right-hand side of (9) describes diffraction, the second one – the second-order dispersion, the third one – the Kerr nonlinearity, the fourth term describes the plasma nonlinearity, and the fifth one – the photoionisation loss. The increase in the pulse wavefront steepness (known as the wave nonstationarity [31]), which makes a noticeable contribution to the transformation of the pulse spectrum and weakly affects the geometrical and energy characteristics of filaments, was neglected. According to the Cauchy formula, the coefficient k''_ω determining the group velocity dispersion in air at 1.24 μm is 0.11×10^{-28} s^2 m^{-1}. The radiation attenuation coefficient in plasma is $\alpha = I^{-1}K\hbar\omega(\partial N_e/\partial t)$, where K is the order of multiphoton ionisation. The pulse shape is assumed Gaussian, its full width at the e^{-1} level being 96 fs. The laser beam at the telescope output was collimated, and the beam intensity profile $I(x, y, z = 0)$ was proportional to the energy density distribution $F(x, y, z = 0)$ measured in the beam cross section (Fig. 4) with the characteristic size 1.4 mm.

The numerical simulation was performed in variables x, y, t, z, because the initial intensity distribution in the beam cross section is not axially symmetric. We used in calcu-

lations a nonuniform network in the x, y plane with a step of 5 μm along both coordinates in the light field localisation region. The step was continuously increased up to 75 μm with moving from the network centre by a distance equal to five radii of the initial beam, a time step being 0.5 fs. The nonlinear system of equations (5)–(9) was solved by the decomposition method with the adaptive digitisation step along the radiation propagation direction. The numerical experiment was performed by using a 2.66-GHz Dual Core Intel Xeon 5150 four-processor computer. For each initial pulse energy W from the range of values specified in experiments, an individual problem was considered, which was solved for ~ 100 hours.

Figure 7 presents the energy density distributions $F(x, y)$ in the beam cross section calculated numerically at the same distances as in experiments for different pulse energies. The calculated energy densities are presented in the same format as those obtained with the help of the CCD camera with the two-photon response at 1.24 μm. As in the laboratory experiment, an axially symmetric mode is formed with increasing energy W, and the laser pulse energy is concentrated at the beam axis. The results of the numerical simulation are in qualitative agreement with experimental data.

Figure 5 presents the radii of the energy density distribution calculated numerically. The radius of the beam cross section was determined by the same method as in experimental data processing. The filament formation energy $W_{\mathrm{fil}}^{\mathrm{calc}}$ found in numerical calculations is 4.5 mJ for the distance $z = 3.12$ m and 3 mJ for $z = 5.92$ m, which is close to experimental results. However, the calculated filament radius is considerably smaller than the experimental radius. This discrepancy is related to errors introduced by the measurement stand during recording the energy density distribution. Indeed, the critical self-focusing power of laser radiation in glass is approximately 500 times lower than in

air. Although the pulse power decreases by more than 25 times after its Fresnel reflection from a glass plate on the measurement stand, the reflected radiation experiences self-focusing in microobjective lenses, and the transverse size of the beam considerable decreases. The diffraction divergence of this radiation in air between the microobjective and CCD camera leads to the overstated value of the measured beam cross section. This error is especially significant for a pulse of energy close to or exceeding the filament formation energy, whose diameter decreases down to a few hundred micrometres.

Figure 6 presents the peak pulse energies obtained in numerical simulations. The deviation of numerical results from experimental data can be explained by the error in the specification of the initial beam profile in simulations.

6. Parameters of filaments formed by radiations from the Cr : forsterite and Ti : sapphire lasers

To compare the parameters of filaments formed by pulsed radiation at 0.8 and 1.24 μm, we performed numerical simulations. We considered two collimated beams with the initial pulse energy 3 mJ and other initial parameters corresponding to experimental conditions. The beam intensity distribution was assumed Gaussian both in the beam cross section and in time.

The parameters of a filament were compared in the region of its start, where the radiation intensity saturated in the central temporal slice of the pulse (Table 1).

According to the results presented in Table 1, the radii of the filament and plasma channel for radiation from the Cr : forsterite laser are 1.6 times greater than for radiation from the Ti : sapphire laser, whereas the peak radiation intensities and energy densities in filaments differ insignificantly. As a result, the filament energy W_{a} determined within the aperture of diameter 500 μm in the case of the
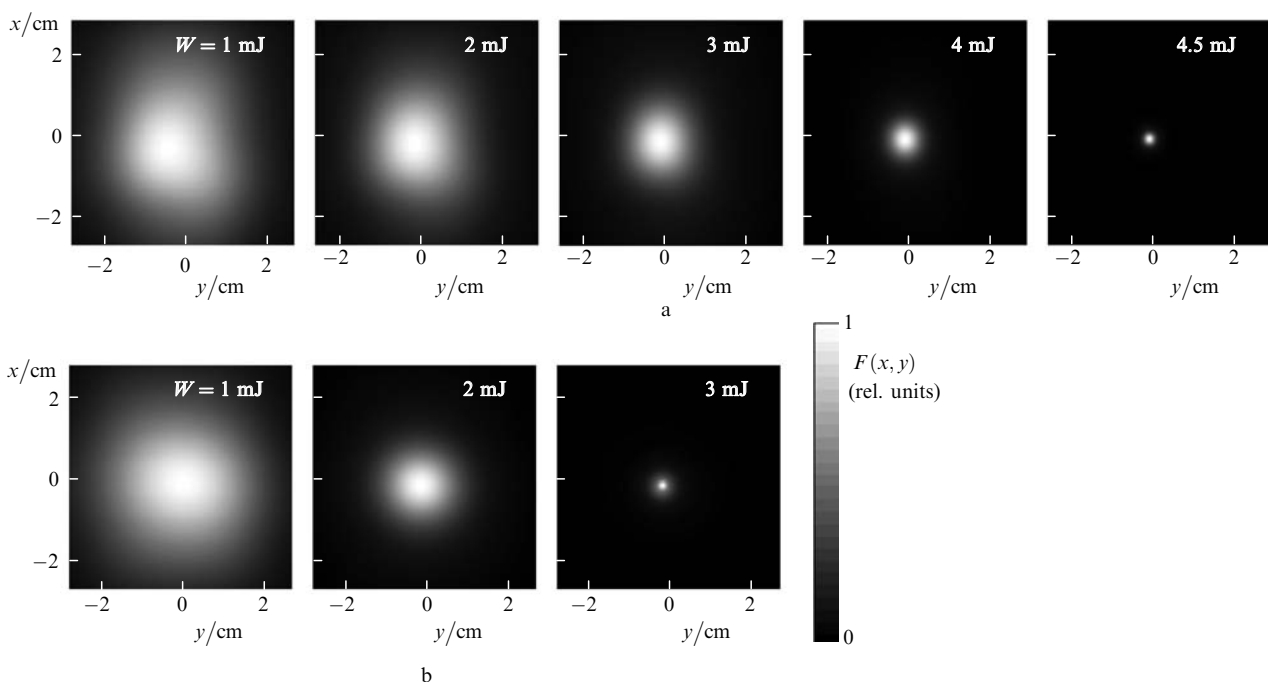

Figure 7. Energy density distributions $F(x, y)$ in the beam cross section calculated numerically at distances $z = 3.12$ (a) and 5.92 m (b) for different pulse energies W. The value of $F(x, y)$ is normalised to the peak value F_{max} for each picture.

Table 1. Parameters of filaments obtained in numerical simulations of filamentation of radiations from the Ti:sapphire and Cr:forsterite lasers.

Laser	$\lambda/\mu m$	z_f/m	$I_{max}/W\ cm^{-2}$	$F_{max}/J\ cm^{-2}$	$r_{fil}/\mu m$	W_a/mJ	N_e^{max}/cm^{-3}	D_e/m^{-1}	$r_{pl}/\mu m$
Ti:sapphire	0.8	2.7	1.4×10^{14}	1.45	81	0.47	7.75×10^{16}	8.5×10^{13}	18
Cr:forsterite	1.24	4	1.2×10^{14}	1.47	127	0.84	2.24×10^{16}	6×10^{13}	29

N o t e s : the full pulse duration at the e^{-1} level is 96 fs; the radius of a Gaussian beam is 1.4 mm (at the e^{-1} level); the energy is 3 mJ; z_f: distance to the filament onset; I_{max}: the peak pulse intensity; r_{fil}: filament radius; W_a: filament energy in the aperture of diameter 500 μm; N_e^{max}: peak electron concentration; D_e: linear electron density; r_{pl}: plasma channel radius (at the e^{-1} level).

Cr:forsterite laser is greater by 80% than for the Ti:sapphire laser. In the case of the 1.24-μm Cr:forsterite laser radiation, the filament is formed at a distance of one and a half greater than in the case of the 0.8-μm Ti:sapphire laser radiation. The electron concentration in the plasma channel of the filament produced by the 1.24-μm radiation is lower than in the plasma channel of the filament produced by the 0.8-μm radiation. In particular, the linear density of the filament plasma when the Cr:forsterite laser is used is lower by 30 % than in the case of the Ti:sapphire laser.

Our analysis showed that the Cr:forsterite laser has certain advantages over the Ti:sapphire laser for providing a higher energy density concentrated in a filament at large distances. Thus, pulsed radiation at 1.24 μm delivers a greater amount of energy by a larger distance than pulsed radiation at 0.8 μm having the same initial pulse energy. These advantages of the Cr:forsterite laser radiation can be useful for applications in the atmospheric optics such as remote probing of atmosphere and spectroscopy of remote target surfaces. In this case, because of a lower electron concentration in the filament channel produced by radiation from the Cr:forsterite laser, a parasitic recombination signal of a laser plasma in air during the spectroscopy of targets is reduced. In problems of controlling electric discharges, the Ti:sapphire laser radiation is preferable because it produces filaments with plasma channels with a higher electron concentration.

7. Conclusions

The filamentation of the pulsed 1.24-μm Cr:forsterite laser radiation has been investigated experimentally and theoretically. The dependences of the peak energy density and filament radius on the initial pulse energy have been obtained. The results of numerical simulation are in qualitative agreement with experimental data, which confirms indirectly the correctness of the filamentation model proposed in the paper. A comparison of the parameters of filaments produced by radiations from the Cr:forsterite and Ti:sapphire lasers has shown that a filament in the Cr:forsteriute laser radiation is formed at a greater distance and contains a greater amount of energy than a filament in the the Ti:sapphire laser radiation. This suggests that the Cr:forsterite laser offers potential advantages for applications in atmospheric optics.

References

1. Kasparian J., Rodriguez M., Mejean G., Yu J., Salmon E., Wille H., Bourayou R., Frey S., Andre Y.-B., Mysyrowicz A., Sauerbrey R., Wolf J.-P., Woste L. *Science*, **301**, 61 (2003).
2. Chin S.L., Hosseini S.A., Liu W., Luo Q., Berge F., Akozbek N., Becker A., Kandidov V.P., Kosareva O.G., Schroeder H. *Can. J. Phys.*, **83**, 863 (2005).
3. Couairon A., Mysyrowicz A. *Phys. Rep.*, **441**, 47 (2007).
4. Berge L., Skupin S., Nuter R., Kasparian J., Wolf J.-P. *Rep. Progr. Phys.*, **70**, 1633 (2007).
5. Kasparian J., Wolf J.-P. *Opt. Express*, **16**, 466 (2008).
6. Mejean G., Kasparian J., Yu J., Frey S., Salmon E., Wolf J.-P. *Appl. Phys. B: Lasers Opt.*, **78**, 535 (2004).
7. Luo Q., Xu H.L., Hosseini S.A., Daigle J.-F., Berge F., Sharifi M., Chin S.L. *Appl. Phys. B: Lasers Opt.*, **82**, 105 (2006).
8. Stelmaszczyk K., Rohwetter P., Mejean G., Yu J., Salmon E., Kasparian J., Ackermann R., Wolf J.-P., Woste L. *Appl. Phys. Lett.*, **85**, 3977 (2004).
9. Liu W., Xu H.L., Mejean G., Kamali Y., Daigle J.F., Azarm A., Simard P.T., Mathieu P., Roy G., Chin S.L. *Spectrochim. Acta. Pt B: At. Spec.*, **62**, 76 (2007).
10. Tzortzakis S., Prade B., Franco M., Mysyrowicz A. *Phys. Rev. E*, **64**, (2001).
11. Rodriguez M., Sauerbrey R., Wille H., Wöste L., Fujii T., André Y.B., Mysyrowicz A., Klingbeil L., Rethmeier K., Kalkner W., Kasparian J., Salmon E., Yu J., Wolf J.-P. *Opt. Lett.*, **27**, 772 (2002).
12. Davis K.M., Miura K., Sugimoto N., Hirao K. *Opt. Lett.*, **21**, 1729 (1996).
13. Golubtsov I.S., Kandidov V.P., Kosareva O.G. *Kvantovaya Elektron.*, **33**, 525 (2003) [*Quantum Electron.*, **33**, 525 (2003)].
14. Méchain G., Couairon A., André Y.B., D'Amico C., Franco M., Prade B., Tzortzakis S., Mysyrowicz A., Sauerbrey R. *Appl. Phys. B: Lasers Opt.*, **79**, 379 (2004).
15. Shlenov S.A., Fedorov V.Yu., Kandidov V.P. *Opt. Atmos. Okean.*, **20**, 308 (2007).
16. La Fontaine B., Vidal F., Jiang Z., Chien C.Y., Comtois D., Desparois A., Johnston T.W., Kieer J.-C., Pepin H. *Phys. Plasmas*, **6**, 1615 (1999).
17. Béjot P., Bonacina L., Extermann J., Moret M., Wolf J.-P., Ackermann R., Lascoux N., Salamé R., Salmon E., Kasparian J., Bergé L., Champeaux S., Guet C., Blanchot N., Bonville O., Boscheron A., Canal P., Castaldi M., Hartmann O., Lepage C., Marmande L., Mazataud E., Mennerat G., Patissou L., Prevot V., Raffestin D., Ribolzi J. *Appl. Phys. Lett.*, **90**, 151106 (2007).
18. Naudeau M.L., Law R.J., Luk T.S., Nelson T.R., Cameron S.M. *Opt. Express*, **14**, 6194 (2006).
19. Agranat M.B., Ashitkov S.I., Ivanov A.A., Konyashchenko A.V., Ovchinnikov A.V., Fortov V.E. *Kvantovaya Elektron.*, **34**, 506 (2004) [*Quantum Electron.*, **34**, 506 (2004)].
20. Agranat M.B., Ashitkov S.I., Ivanov A.A., Konyashchenko A.V., Ovchinnikov A.V., Podshivalov A.A. *Kvantovaya Elektron.*, **34**, 1018 (2004) [*Quantum Electron.*, **34**, 1018 (2004)].
21. Ovchinnikov A.V., Ashitkov S.I., Agranat M.B., Sitnikov D.S. *Kvantovaya Elektron.*, **38**, 325 (2008) [*Quantum Electron.*, **38**, 325 (2008)].
22. Prade B., Franco M., Mysyrowicz A., Couairon A., Buersing H., Eberle B., Krenz M., Seier D., Vasseur O. *Opt. Lett.*, **31**, 2601 (2006).
23. Kandidov V.P., Kosareva A.G., Koltun A.A. *Kvantovaya Elektron.*, **33**, 69 (2003) [*Quantum Electron.*, **33**, 69 (2003)].
24. Brodeur A., Chien C.Y., Ilkov F.A., Chin S.L., Kosareva O.G., Kandidov V.P. *Opt. Lett.*, **22**, 304 (1997).
25. Fedorov V.Yu., Kandidov V.P. *Opt. Spektrosk.*, **105**, 306 (2008).
26. Oleinikov P.A., Platonenko V.T. *Laser Phys.*, **3**, 618 (1993).

27. Chiron A., Lamouroux B., Lange R., Ripoche J.F., Franco M., Prade B., Bonnaud G., Riazuelo G., Mysyrowicz A. *Eur. Phys. J. D*, **6**, 383 (1999).
28. Mlejnek M., Wright E.M., Moloney J.V. *Opt. Lett.*, **23**, 382 (1998).
29. Perelomov A.M., Popov V.S., Terent'ev M.V. *Zh. Eksp. Teor. Fiz.*, **51**, 309 (1966).
30. Talebpour A., Yang J., Chin S.L. *Opt. Commun.*, **163**, 29 (1999).
31. Akhmanov S.A., Vysloukh V.A., Chirkin A.S. *Optika femtosekundnykh lazernykh impul'sov* (Optics of Femtosecond Laser Pulses) (Moscow: Nauka, 1988).